Acoustically-driven surface and hyperbolic plasmon-phonon polaritons in graphene/h-BN heterostructures on piezoelectric substrates

R Fandan[1,2], J Pedrós[1,2], J Schiefele[3], A Boscá[1,2], J Martínez[1,4] and F Calle[1,2]

[1] Instituto de Sistemas Optoelectrónicos y Microtecnología, Universidad Politécnica de Madrid, Av. Complutense 30, Madrid 28040, Spain
[2] Departamento de Ingeniería Electrónica, E.T.S.I de Telecomunicación, Universidad Politécnica de Madrid, Av. Complutense 30, Madrid 28040, Spain
[3] Instituto de Ciencia de Materiales de Madrid, Consejo Superior de Investigaciones Científicas, C/ Sor Juana Inés de la Cruz 3, Madrid 28049, Spain
[4] Departamento de Ciencia de Materiales, E.T.S.I de Caminos, Canales y Puertos, Universidad Politécnica de Madrid, C/ Profesor Aranguren s/n, Madrid 28040, Spain

E-mail: rajveer.fandan@upm.es and j.pedros@upm.es

Abstract

Surface plasmon polaritons in graphene couple strongly to surface phonons in polar substrates leading to hybridized surface plasmon-phonon polaritons (SPPPs). We demonstrate that a surface acoustic wave (SAW) can be used to launch propagating SPPPs in graphene/h-BN heterostructures on a piezoelectric substrate like AlN, where the SAW-induced surface modulation acts as a dynamic diffraction grating. The efficiency of the light coupling is greatly enhanced by the introduction of the h-BN film as compared to the bare graphene/AlN system. The h-BN interlayer not only significantly changes the dispersion of the SPPPs but also enhances their lifetime. The strengthening of the SPPPs is shown to be related to both the higher carrier mobility induced in graphene and the coupling with h-BN and AlN surface phonons. In addition to surface phonons, hyperbolic phonons polaritons (HPPs) appear in the case of multilayer h-BN films leading to hybridized hyperbolic plasmon-phonon polaritons (HPPPs) that are also mediated by the SAW. These results pave the way for engineering SAW-based graphene/h-BN plasmonic devices and metamaterials covering the mid-IR to THz range.

Keywords: graphene, surface plasmon phonon polariton, surface acoustic waves, h-BN, hyperbolic polaritons

(Some figures may appear in colour only in the online journal)

1. Introduction

Surface plasmon polaritons (SPPs) are electromagnetic waves confined to the interface between two materials and accompanied by collective oscillations of surface charges. One of the most intriguing properties of SPPs is that their momentum is larger than that corresponding to free photons of the same frequency [1]. As a consequence, SPPs are bound modes whose fields decay exponentially away from the interface, exhibiting deep subwavelength confinement which results in strong light–matter interaction [2, 3]. Thus, SPPs in metals have attracted a strong interest over the last few decades for manipulating light and light–matter interactions at scales well beyond the diffraction limit [4] and have laid the foundation

of a whole new range of fields including SPP-based nanophotonic devices [5, 6], metamaterials [7], metasurfaces [8], and quantum plasmonics [9]. However, the lifetime of SPPs in metals is extremely short when the light is confined to deep subwavelength scales and their properties cannot be modulated *in situ* [10, 11]. In the case of doped graphene, SPPs can be confined to extreme subwavelength scales while preserving a long lifetime [10]. The carriers in graphene interact strongly with the surface optical (SO) phonons of polar substrates via the long-range Fröhlich coupling leading to hybridized surface plasmon-phonon polaritons (SPPPs) [12, 13]. Moreover, unlike metals, the SPP (or SPPP) wavelength in graphene can be tuned *in situ* through the modulation of the carrier density by electrostatic gating, thus providing a versatile plasmonic platform covering the mid-IR to THz range [14–16]. Hence, graphene plasmonics are being investigated for a large number of applications including 2D transformation optics [17], optical signal processing [17, 18], single photon nonlinear optics [19], biosensing [20], and integrated optics [21].

In order to excite a SPP (or SPPP) in graphene, a large momentum mismatch has to be overcome. Momentum can be gained either using near-field techniques [22–24], frequency mixing [25], or diffraction at nanostructures using far-field radiation, where the nanostructures can be made by patterning the graphene film itself [12, 26, 27] or the substrate where the graphene layer is transferred to [28, 29]. Surface acoustic waves (SAWs) have been shown to provide a suitable mechanism to launch propagating SPPPs in unpatterned graphene using simple far-field excitation [30]. An interdigital transducer (IDT) on a piezoelectric film is used to launch the SAW across the graphene sheet creating a tunable optical grating without the need of any patterning in either the graphene layer or the substrate, thus eliminating edge scattering and fragility issues. In addition to these advantages, the use of IDTs enables the fabrication of graphene plasmonic devices by the microelectronics industry, as compared to other schemes using an external mechanical vibrator [31]. Moreover, the use of IDTs permits to efficiently control the SPPP both temporally and spatially. Thus, the propagating SPPP can be switched electrically via the high-frequency signal at the IDT and its wavefront can be shaped by tailoring the IDT design. For example, curved IDTs creating interfering SAWs could be used for focusing the SPPP.

In this paper, we provide a complete simulation study of graphene SPPPs excited by means of a SAW in graphene/h-BN/AlN heterostructures with varying h-BN film thickness. The atomically flat surface without dangling bonds of h-BN is known to provide the largest carrier mobility in graphene as compared to any other insulating substrate [32–34]. We show that the introduction of an h-BN film between the graphene and the AlN substrate not only enhances the SPPP lifetime, but also significantly changes the hybridized SPPP dispersion, as compared to the previously studied graphene/AlN system [30]. The lifetime enhancement provided by the h-BN interlayer is shown to be related to both the higher carrier mobility in graphene and the larger lifetime of the surface phonons as compared to the AlN substrate. In addition, hyperbolic phonons polaritons (HPPs) appear in the case of multilayer h-BN films, presenting high confinement ratios and quality factors

[35]. HPPs in multilayer h-BN are difficult to modulate but when coupled with the graphene carriers, leading to hybridized hyperbolic plasmon-phonon polaritons (HPPPs), they can be modulated by changing the Fermi energy of graphene. The HPPPs in graphene/h-BN have been demonstrated to have minimal ohmic losses and propagation lengths two times greater than that of HPPs in bare h-BN [24, 36]. We demonstrate that a SAW can also be used to couple light into HPPPs in the graphene/h-BN/AlN systems.

2. Optical properties of graphene, h-BN, and AlN

The frequency-dependent conductivity of graphene in the local limit $(k \to 0)$ and for $\omega \gg \tau_e^{-1}$ can be calculated using the Kubo formula [37] as

$$
\sigma(\omega) = \frac{e^2 \left(\omega + i\tau_e^{-1}\right)}{i\pi\hbar^2} \left[\frac{1}{\left(\omega + i\tau_e^{-1}\right)^2} \right.
$$
$$
\times \int_0^\infty E\left(\frac{\partial F(E)}{\partial E} - \frac{\partial F(-E)}{\partial E}\right) dE
$$
$$
\left. + \int_0^\infty \frac{F(E) - F(-E)}{\left(\omega + i\tau_e^{-1}\right)^2 - 4(E/\hbar)^2} dE \right], \quad (1)
$$

where $F(E) = [\exp\{(E - \mu_c)/k_B T\} + 1]^{-1}$ is the Fermi-Dirac distribution, μ_c is the chemical potential and τ_e is the electron relaxation time. τ_e is related to the mobility, μ, and the Fermi energy, E_F, by $\tau_e = \mu E_F v_F^{-2}$ where v_F is the Fermi velocity of 10^6 ms^{-1}. The first and second terms in equation (1) represent the contributions of the intraband $(\hbar\omega < 2E_F)$ and interband $(\hbar\omega \geqslant 2E_F)$ transitions, respectively, as shown in figure 1(a).

h-BN is an anisotropic van der Waals crystal with two IR active phonon modes: the in-plane (∥) A_{2u} phonon modes, with frequencies $\omega_{TO\parallel} = 0.096$ eV and $\omega_{LO\parallel} = 0.102$ eV, and the out-of-plane (⊥) E_{1u} phonon modes, with frequencies $\omega_{TO\perp} = 0.169$ eV and $\omega_{LO\perp} = 0.199$ eV [36]. The frequency-dependent relative permittivity of h-BN is given by [36]

$$
\epsilon_m(\omega) = \epsilon_{\infty,m}\left(\frac{\omega_{LO\,m}^2 - \omega_{TO\,m}^2}{\omega_{TO\,m}^2 - i\gamma_m\omega - \omega^2}\right), \quad (2)
$$

where $m = \parallel, \perp$; $\epsilon_{\infty,\parallel} = 2.95$ and $\epsilon_{\infty,\perp} = 4.87$ are the high-frequency dielectric constants; and $\gamma_\parallel = 0.49$ meV and $\gamma_\perp = 0.62$ meV are the damping frequencies [36]. The permittivity of h-BN becomes negative in the frequency range between the TO and LO phonons $(\omega_{TO\,m} < \omega < \omega_{LO\,m})$, leading to two reststrahlen bands. The opposite sign in the in-plane and out-of-plane components within these bands makes h-BN a hyperbolic material. The lower band presents type-I hyperbolicity $(\mathrm{Re}(\epsilon_\parallel) < 0, \mathrm{Re}(\epsilon_\perp) > 0)$, whereas the upper band has type-II hyperbolicity $(\mathrm{Re}(\epsilon_\parallel) > 0, \mathrm{Re}(\epsilon_\perp) < 0)$, as shown in figure 1(b).

AlN is only slightly anisotropic [38] as compared to h-BN. Thus, for simplicity, we assume an isotropic behaviour with a unique reststrahlen band located between $\omega_{TO} = 0.083$ eV and $\omega_{LO} = 0.111$ eV, as shown in figure 1(b). The frequency-dependent relative permittivity of AlN is given by
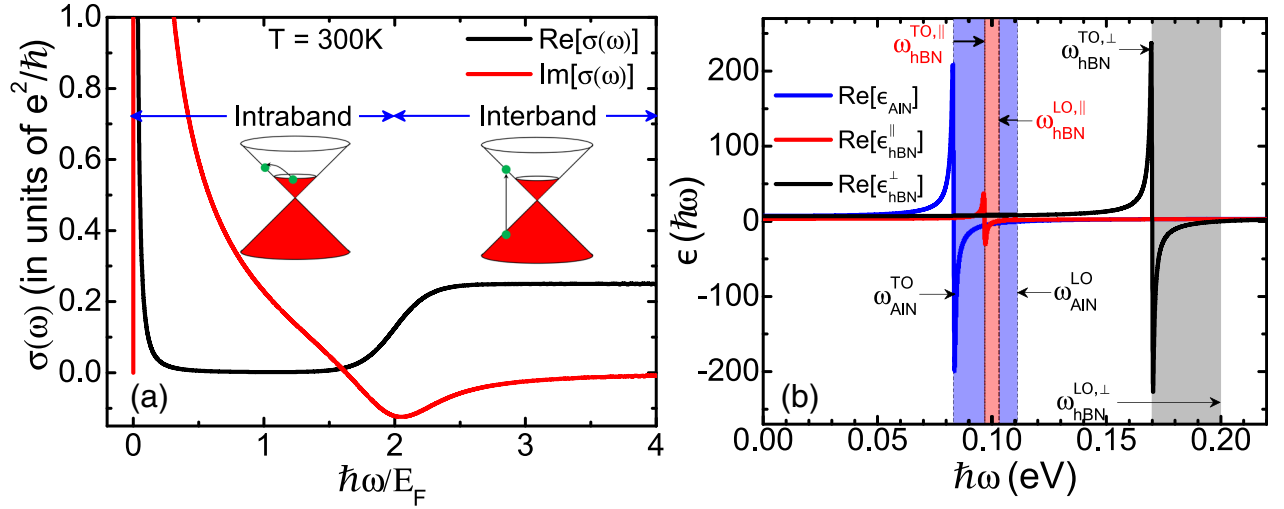
Figure 1. (a) Conductivity of graphene as a function of the photon energy normalized by the Fermi energy. The contribution from the intraband and interband transitions is indicated. (b) Permittivity of h-BN and AlN graphene as a function of the photon energy. Shaded regions are the reststrahlen bands, which appear in the frequency ranges between the TO and LO phonons.

$$\epsilon\left(\omega\right) = \epsilon_\infty + \left(\epsilon_0 - \epsilon_\infty\right)\left(\frac{\omega_{TO}^2}{\omega_{TO}^2 - i\gamma\omega - \omega^2}\right), \quad (3)$$

where $\epsilon_0 = 7.37$ and $\epsilon_\infty = 3.93$ are the static and high-frequency dielectric constants, respectively, and $\gamma = 0.64\,\mathrm{meV}$ is the damping frequency [39].

3. Dispersion of SPPPs and HPPPs in graphene/h-BN/AlN systems

The carriers in graphene couple to the long-range electric field induced by optically active phonons in the surrounding materials. Both h-BN and AlN are polar materials, so that their SO

phonons strongly couple to graphene carriers. Thus, graphene carriers can interact by exchange of SO phonons leading to a potential given by [34]

$$V_{\omega_{SO}}\left(k,\omega\right) = \frac{4\pi\hbar\alpha c}{2k}\sum_{SO}\frac{e^{-2kz}a\omega_{SO}^2}{\left(\omega + i\tau_{SO}^{-1}\right)^2 - \omega_{SO}^2}, \quad (4)$$

where k, ω_{SO}, and τ_{SO} are the SO phonon wave vector, frequency, and lifetime, respectively, z is the graphene-substrate separation, $a = \left(\epsilon_0 - \epsilon_\infty\right)/\left[\left(1 + \epsilon_0\right)\left(1 + \epsilon_\infty\right)\right]$, $\alpha = 1/137$ is the fine-structure constant, and c is the velocity of the light

in vacuum. τ_{SO} is estimated as the inverse of the damping rate of TO phonon, whereas ω_{SO} is the solution of the equation $\epsilon\left(\omega\right) + 1 = 0$.

Apart from the coupling to substrate phonons from the surrounding materials, carriers in graphene also couple to in-plane optical and out-of-plane (flexural) phonon modes in the graphene sheet itself. While the former would play a role only at plasmon energies above $0.2\,\mathrm{eV}$ [12], the latter is strongly suppressed in substrate supported graphene sheets [40, 41]. Hence, we have neglected here the coupling to both of these phonons.

The total effective carrier interaction results from Coulomb interaction, $V_c\left(k\right)$, given by [42]

$$V_c\left(k\right) = \frac{e^2\left(\left(\epsilon_{hBN}^{\infty,\perp}\,\epsilon_{hBN}^{\infty,\parallel}\right)^{1/2} + \epsilon_{AlN}^\infty\tanh\left[kd\left(\epsilon_{hBN}^{\infty,\perp}/\epsilon_{hBN}^{\infty,\parallel}\right)^{1/2}\right]\right)}{k\epsilon_{vac}\left(\left(\epsilon_{hBN}^{\infty,\perp}\,\epsilon_{hBN}^{\infty,\parallel}\right)^{1/2} + \left(\frac{\epsilon_{AlN}^\infty + \epsilon_{hBN}^{\infty,\perp}\,\epsilon_{hBN}^{\infty,\parallel}}{1 + \epsilon_{AlN}^\infty}\right)\tanh\left[kd\left(\epsilon_{hBN}^{\infty,\perp}/\epsilon_{hBN}^{\infty,\parallel}\right)^{1/2}\right]\right)} \quad (5)$$

(with $\epsilon_{vac} = e^2/\left(4\pi\hbar\alpha c\right)$ the permittivity of vacuum and d is the thickness of h-BN) and phonon exchange, $V_{\omega_{SO}}\left(k,\omega\right)$. Within the random phase approximation (RPA), the total effective carrier interaction $V_{RPA}^{eff}\left(k,\omega\right)$ is given by [12, 13]

$$V_{RPA}^{eff}\left(k,\omega\right) = \frac{V_c\left(k\right)}{\epsilon_{RPA}} = \frac{V_c\left(k\right) + V_{\omega_{SO}}\left(k,\omega\right)}{1 - \left(V_c\left(k\right) + V_{\omega_{SO}}\left(k,\omega\right)\right)\prod_{\rho\rho}^0\left(k,\omega\right)}, \quad (6)$$

where ϵ_{RPA} is the total dielectric screening function and $\prod_{\rho\rho}^0\left(k,\omega\right)$ is the non-interacting part (i.e. the pair-bubble
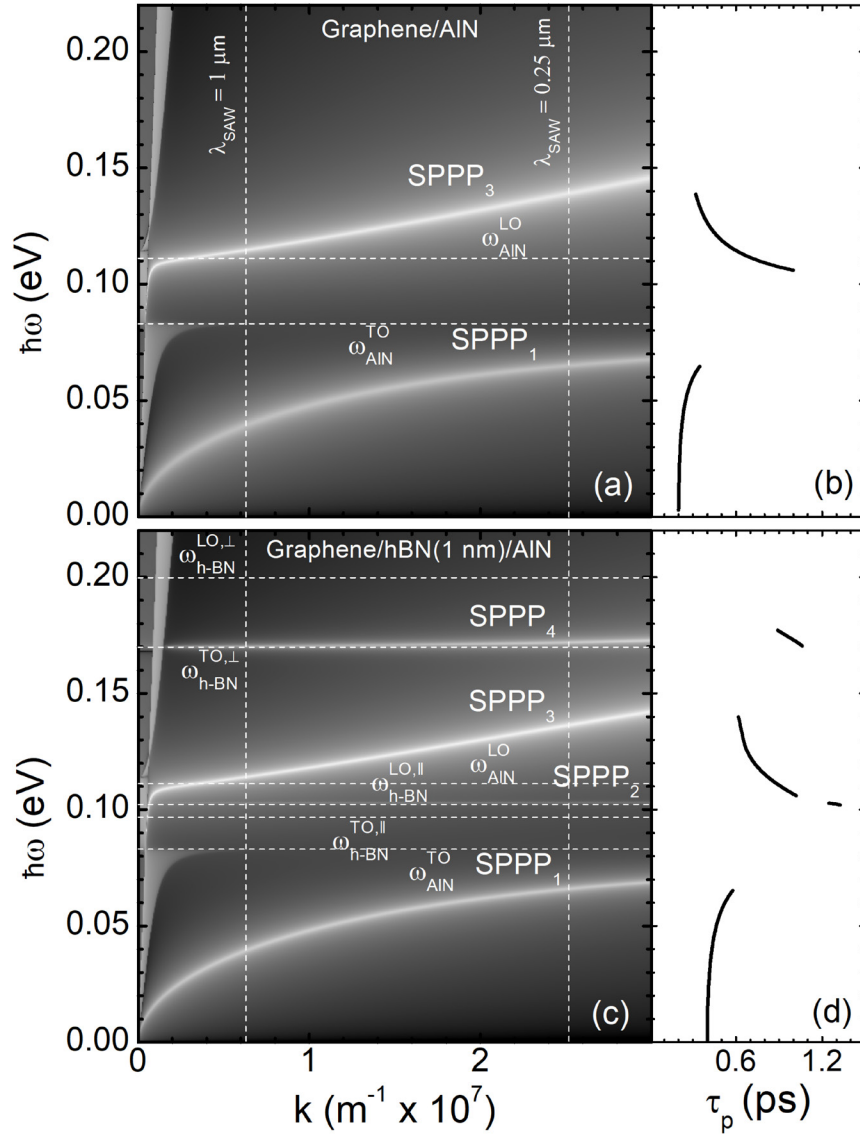
Figure 2. SPPP$_i$ dispersion for (a) graphene/AlN and (c) graphene/h-BN/AlN with an h-BN film thickness $d = 1$ nm. Parameters are $E_F = 0.4$ eV for both structures and $\mu = 5000$ and $10\,000$ cm^2 V^{-1} s^{-1} for graphene/AlN and graphene/hBN/AlN, respectively. Dashed horizontal lines correspond to the phonon frequencies of AlN and h-BN, whereas the dashed vertical lines indicate SAW wavelengths λ_{SAW} of 0.25 and 1 μm. (b), (d) lifetime of the SPPP$_i$.

diagram) of the charge-charge correlation function (2D polarizability). The latter is given by the modified Lindhard function [43, 44]

$$\prod_{\rho\rho}^{0} (k, \omega) = -\frac{g_s g_v}{4\pi^2} \int d^2q \sum_{ss'} f_{ss'} (q, q+k)$$

$$\times \frac{F(E_s(q)) - F(E_{s'}(|q+k|))}{E_s(q) - E_{s'}(|q+k|) + \hbar\omega + i\hbar\tau_e^{-1}}, \quad (7)$$

where $g_s = g_v = 2$ are the spin and valley degeneracies, respectively, $s, s' = \pm 1$ denote the band indices, $E_{\pm}(q) = \pm \hbar v_F q - \mu_c$ are the eigenenergies, $F(E_s(q)) = [\exp\{E_s(q)/k_B T\} + 1]^{-1}$ is the Fermi-Dirac distribution, and $f_{ss'}(q, q+k)$ is the band overlap of the wavefunction. The latter term includes the characteristic difference between the polarizability of the Dirac (massless) electron gas in

graphene and a Fermi (massive) 2D electron gas in a semiconductor system. It is given by the expression [43, 44]

$$f_{ss'}(q, q+k) = \frac{1}{2}\left(1 + ss'\frac{q + k\cos\theta}{|q+k|}\right), \quad (8)$$

where θ is the angle between q and $q + k$. In the limit $\omega > v_F k$ and $E_F \gg \min(\hbar\omega, T)$, $\prod_{\rho\rho}^{0}(k, \omega)$ can be approximated to [26]

$$\prod_{\rho\rho}^{0} (k, \omega) \approx \frac{E_F k^2}{\pi\hbar^2(\omega + i\tau_e^{-1})^2}. \quad (9)$$

The electron energy loss function $L(k, \omega) = -\text{Im}[1/\epsilon_{RPA}(k, \omega)]$ characterizes the spectral density of collective charge excitations. The SPPP dispersion can be obtained by solving the equation $\epsilon_{RPA}(k, \omega) = 0$, corresponding to the poles of
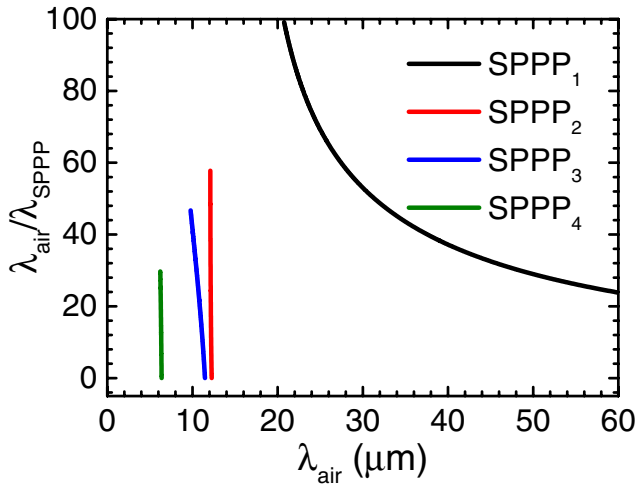
Figure 3. Confinement ratio $\lambda_{\text{air}}/\lambda_{\text{SPPP}}$ for the different SPPP$_i$ supported by the graphene/h-BN ($d = 1$ nm)/AlN system. Parameters are $E_F = 0.4$ eV and $\mu = 10\,000$ cm^2 V^{-1} s^{-1}.

$L(k, \omega)$. The lifetime of the SPPP, τ_p can be calculated by solving the equation $\epsilon_{RPA}\left(k, \omega_p - i\tau_p^{-1}\right) = 0$.

Figures 2(a) and (c) depict the SPPP dispersion for the graphene/AlN and graphene/h-BN/AlN systems, respectively, where the latter has a 1 nm-thick h-BN interlayer. The graphene mobility has been considered to be enhanced by the h-BN film from $\mu = 5000$ to $10\,000$ cm^2 V^{-1} s^{-1}, whereas $E_F = 0.4$ eV has been set for both cases. The dispersion of the graphene/h-BN/AlN system presents a larger number of SPPP$_i$ as compared to the graphene/AlN counterpart, since the electron-phonon interaction involves both h-BN and AlN surface phonons. In particular, SPPP$_1$ and SPPP$_3$ arise from the interaction of the graphene SPP with the SO phonon in AlN [30], as shown in figures 2(a) and (c), whereas the additional SPPP$_2$ and SPPP$_4$ in figure 2(c) arise, respectively, from the interaction with the $\parallel$ and $\perp$ SO phonons of h-BN. Figures 2(b) and (d) depict the lifetime of the SPPP$_i$ in figures 2(b) and (d), respectively. The hybridized SPPP$_i$ present different spectral weight and lifetime, which depend on the oscillator strength and phonon lifetime of the underlying materials. The lifetime τ_p of the SPPP$_i$ spans between the limits imposed by the graphene carrier relaxation time, τ_e, and the SO phonon lifetime, τ_{SO}. Since the h-BN film enhances the graphene carrier mobility, and hence τ_e, the τ_p of SPPP$_1$ and SPPP$_3$ is increased. On the other hand, h-BN supports longer-lived SO phonons than AlN, providing SPPP$_2$ and SPPP$_4$ with the largest τ_p values (up to almost 1.4 ns for SPPP$_2$, an increase of 40% as compared to values in the graphene /AlN system). Thus, the h-BN interlayer allows both to increase the lifetime of the SPPPs and to broaden the energy range that they cover. The case of SPPP$_2$ is especially interesting. Since the lower reststrahlen band (type-I) of h-BN lies within the reststrahlen band of AlN, the SPPP$_2$ branch is weak in intensity though its proximity to the SO phonon of the h-BN provides it with the largest lifetime. The intensity of SPPP$_2$ is expected to be enhanced if the reststrahlen band of the piezoelectric substrate does not overlap that of the h-BN, as would occur for example with ZnO [30].

The graphene/AlN system permits to achieve deep sub-wavelength confinement of the radiation. With the addition of h-BN, a broader range of energy for confinement can be covered. Figure 3 presents the confinement ratio $\lambda_{\text{air}}/\lambda_{\text{SPPP}}$ as a function of the incident light wavelength λ_{air}. The mid-IR to THz range can be covered with confinement ratios of up to two orders of magnitude.

The dispersion of the graphene/h-BN/AlN system strongly depends on the thickness d of the h-BN interlayer, as shown in figure 4. As d increases, SPPP$_1$ and SPPP$_4$ shift towards higher energies, whereas SPPP$_3$ shifts towards lower energies, and SPPP$_2$ does not vary substantially, as shown in figures 2(c), 4(a) and (b) for $d = 1$, 5, and 10 nm, respectively. For $d = 50$ and 70 nm, see figures 4(c) and (d) respectively, HPPPs [24, 40] appear within the h-BN reststrahlen bands as a result of the natural hyperbolicity of h-BN. These HPPPs appear also in the dispersion of the thinner multilayer h-BN films considered here but at higher k values than those depicted in figures 2(c), 4(a) and (b). In general, the thicker the h-BN interlayer, the stronger its influence on the dispersion curve of the graphene/h-BN/AlN system, with the HPPP$_i$ appearing at lower k values, and the weaker the influence of the AlN susbstrate. Also, increasing the thickness of the h-BN interlayer from 50 to 70 nm, a transition from SPPP$_3$ to SPPP$_2$ is observed, as shown in figures 4(e) and (f). This crossover is also attributed to the fact that, increasing the h-BN thickness the influence of the AlN substrate weakens, while that of the h-BN interlayer strengthens. In summary, by increasing the h-BN thickness the dispersion of the three-layer system (graphene/h-BN/AlN) seems to move gradually towards an effective two-layer system (graphene/h-BN).

SPPPs and HPPPs lead to enhanced absorption of the incident light. The transmittance and reflectance of the graphene/h-BN/AlN system can be calculated from the Fresnel reflection and transmission coefficients by means of the transfer matrix method [45]. Hence, the transfer matrix is given by $M = B_{01}PB_{12}$, where B_{01} and B_{12} are the transfer matrices for the air/h-BN and h-BN/AlN interfaces, respectively, and P is the propagation matrix. These matrices are given by the expressions

$$B_{01} = \begin{pmatrix} 1 + \sigma(\omega)/Z_1 + Z_0/Z_1 & 1 - \sigma(\omega)/Z_1 - Z_0/Z_1 \\ 1 + \sigma(\omega)/Z_1 - Z_0/Z_1 & 1 - \sigma(\omega)/Z_1 + Z_0/Z_1 \end{pmatrix}$$

(10.1)

$$B_{12} = \begin{pmatrix} 1 + Z_1/Z_2 & 1 - Z_1/Z_2 \\ 1 - Z_1/Z_2 & 1 + Z_1/Z_2 \end{pmatrix}$$

(10.2)

$$P = \begin{pmatrix} e^{-ik_1^z d} & 0 \\ 0 & e^{ik_1^z d} \end{pmatrix},$$

(10.3)

where $j = 0$, 1, 2 for air, h-BN, and AlN respectively, $Z_j = \omega \varepsilon_j^{\perp}\left(k_j^z\right)^{-1}$ is the impedance of jth material, where $k_j^z = \left[\varepsilon_j^{\perp}\left((\omega/c)^2 - k^2/\varepsilon_j^{\parallel}\right)\right]^{-1/2}$, and $\sigma(\omega)$ is the conductivity of graphene defined in equation (1).
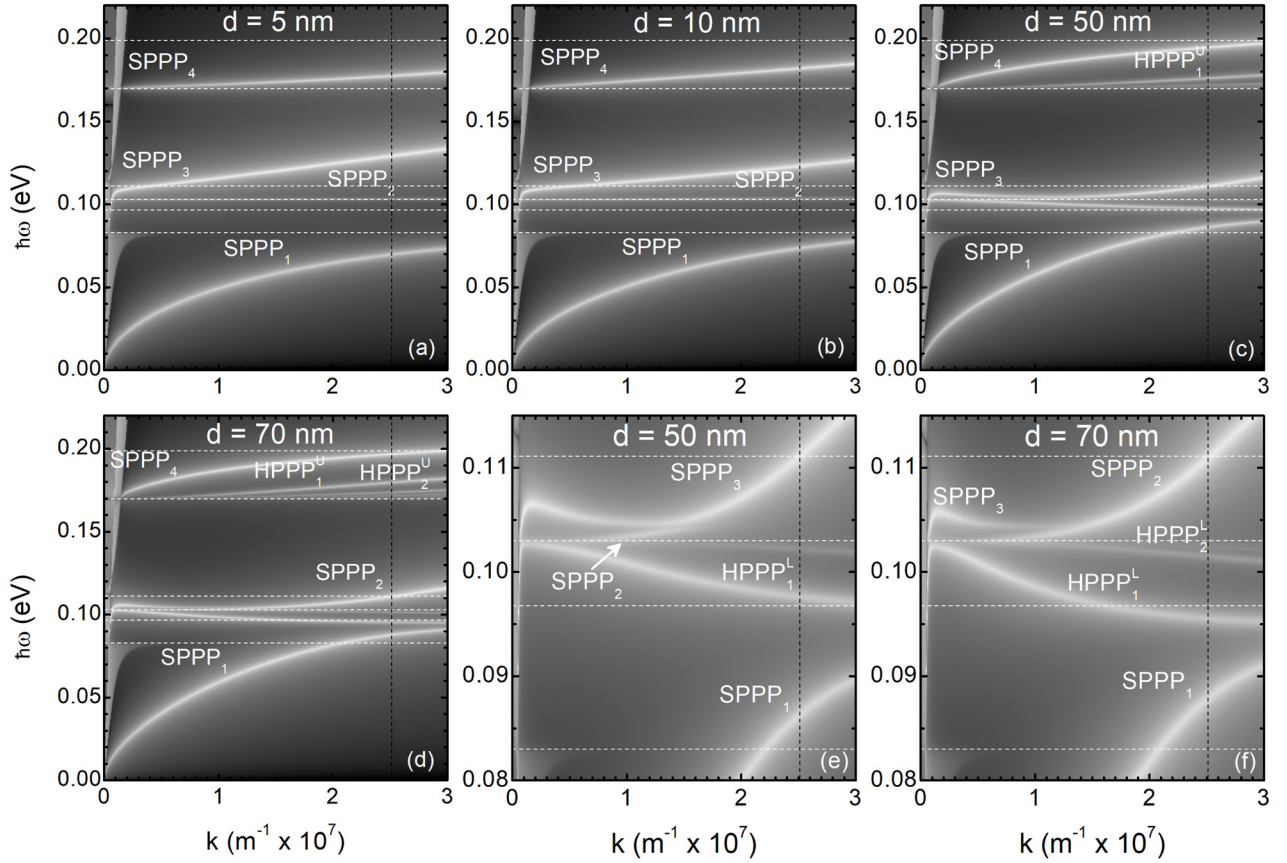
Figure 4. $SPPP_i$ and $HPPP_i^{U,L}$ dispersion for the graphene/h-BN/AlN system with h-BN interlayer thickness d of (a) 5 nm, (b) 10 nm, (c) 50 nm, and (d) 70 nm. (e) and (f) are magnified views of the part of figures (c) and (d), respectively, around the AlN reststrahlen band where a transition from $SPPP_3$ to $SPPP_2$ can be observed. The superscripts in $HPPP_i^{U,L}$ denote the upper and lower reststrahlen bands. Parameters are $E_F = 0.4$ eV and $\mu = 10\,000$ cm^2 V^{-1} s^{-1}. Dashed horizontal white lines correspond to the phonon frequencies of AlN and h-BN, as labelled in figure 2, whereas the dashed vertical line corresponds to a k value given by a $\lambda_{SAW} = 0.25$ μm.
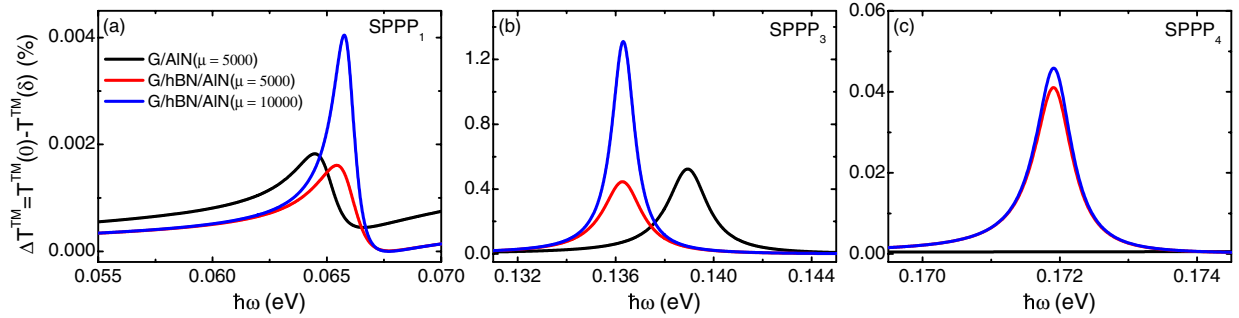

Figure 5. ΔT^{TM} spectra of (a) $SPPP_1$, (b) $SPPP_3$, and (c) $SPPP_4$ for the graphene/AlN and graphene/h-BN($d = 1$ nm)/AlN systems in the presence of a SAW ($m = 1$, $\delta = 4$ nm, and $\lambda_{SAW} = 250$ nm) for variable carrier mobility μ (in units of cm^2 V^{-1} s^{-1}) and $E_F = 0.4$ eV.

For TM-polarized light, the Fresnel reflection (r_{TM}) and transmission (t_{TM}) coefficients are given in terms of elements of the transfer matrix M as $r_{TM} = M_{21}/M_{11}$ and $t_{TM} = 1/M_{11}$. The absorption of the light is given by Im[r_{TM}], which is interpreted as the contour plot of electron energy loss function in figures 2 and 4.

4. SAW-mediated SPPPs and HPPPs

The wave vector mismatch between the light and the SPPPs and HPPPs in the graphene/h-BN/AlN system can be overcome using an IDT on the surface of the AlN substrate to

launch a SAW propagating across the graphene/h-BN heterostructure. The SAW produces a sinusoidal deformation of the surface creating a virtual dynamic diffraction grating that provides the extra wave vector required for the light to couple into the SPPPs [34] and HPPPs. Thus, in the presence of a SAW of wavelength λ_{SAW} and amplitude δ, the transmittance of TM-polarized light is reduced as the SAW-induced diffraction grating scatters the incident light with wave vector $(k_{\|0}, k_{z0})$ into the various diffraction orders $(k_{\|m}, k_{zm})$ with

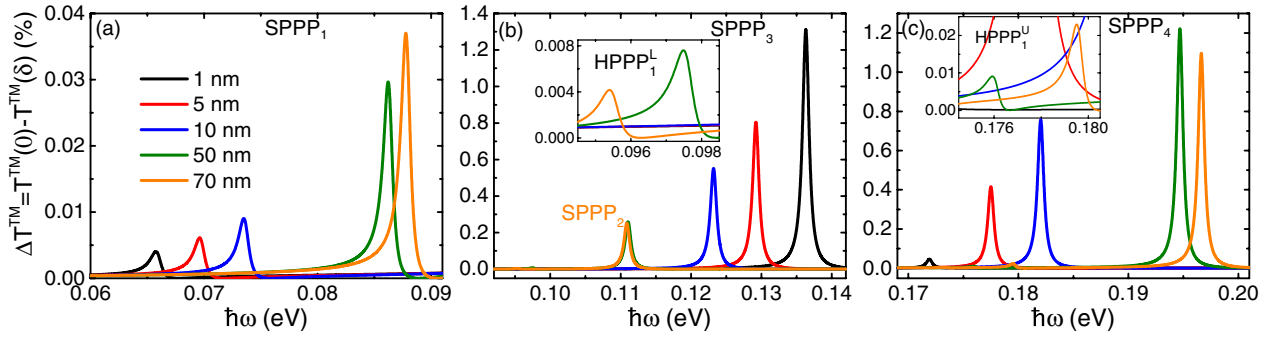$$k_{\|m} = (\omega/c)\sin\theta + m2\pi/\lambda_{SAW}, \tag{11}$$

J. Phys. D: Appl. Phys. **51** (2018) 204004

R Fandan *et al*

Figure 6. ΔT^{TM} spectra of (a) SPPP$_1$, (b) SPPP$_3$ (and SPPP$_2$), and (c) SPPP$_4$ for the graphene/h-BN/AlN systems with $\mu = 10\,000\,cm^2\,V^{-1}\,s^{-1}$, $E_F = 0.4\,eV$ and various h-BN film thickness d in the presence of a SAW ($m = 1$, $\delta = 4\,nm$, and $\lambda_{SAW} = 250\,nm$). For $d = 70\,nm$, SPPP$_2$ mode appears instead of SPPP$_3$. The insets in (b) and (c) show magnified views of the energy range where HPPP$_1^L$ and HPPP$_1^U$ appear, respectively.

$$k_{zm} = \sqrt{(\omega/c)^2 - k_{\|m}^2}, \qquad (12)$$

where θ is the angle of off-normal incidence and m is an integer. The intensity of the diffracted light in mth order, normalized to the intensity of the incoming beam, is given by [46]

$$I^m = \left| r_{TM} J_m \left(2k_{z0}\delta \right) \left[1 + \frac{m\pi}{\lambda_{SAW} k_{zm}} \frac{1 + r_{TM}}{r_{TM}} \right] \right|^2, \quad (13)$$

where J_m is the Bessel function for the mth diffraction order.

Figure 5 plots the change in the transmission, $\Delta T^{TM} = T^{TM}(0) - T^{TM}(\delta)$, in the graphene/AlN and graphene/h-BN($d = 1\,nm$)/AlN systems for the first diffraction order ($m = 1$) induced by a SAW with $\delta = 4\,nm$ and $\lambda_{SAW} = 250\,nm$ due to the generation of SPPPs. SAWs with such amplitude can be achieved by using unidirectional focusing IDTs [47, 48] that provide a large RF power to SAW amplitude conversion efficiency. It has to be noted that ΔT^{TM} has been selected as figure of merit, instead of the more usual extinction coefficient $1 - T^{TM}(\delta)/T^{TM}(0)$, to avoid misleading variations in the values of the later, not related to the variation of the strength of the modes but produced by the normalization by $T^{TM}(0)$ at the boundaries of the reststrahlen bands, where the background signal changes abruptly. As described in the previous section, the SPPP dispersion of the graphene/AlN system is modified by the introduction of a thin h-BN interlayer. This is also reflected into the ΔT^{TM} spectra, as shown in figures 5(a) and (b) for the SPPP$_1$ and SPPP$_3$, respectively. In addition to a frequency shift of the peaks, the enhancement of the mobility induced by the h-BN leads to an increase in the peak intensity and to a reduced full width at half maxima of the peaks. This indicates that the h-BN strengthens SPPP$_1$ and SPPP$_3$ and allows them to live longer and propagate longer distances. Furthermore, new SPPPs appear in the ΔT^{TM} spectra, as shown for example in figure 5(c) for the SPPP$_4$. However, the increase in the mobility induced by the h-BN only enhances slightly the SPPP$_4$. This different behaviour, as compared to SPPP$_1$ and SPPP$_3$, can be explained considering that, as mentioned in the previous section, the lifetime τ_p of the SPPP$_i$ spans in between the limits imposed by τ_e and τ_{SO}. Thus, the closer the SPPP$_i$ to a phonon in the dispersion curve, the stronger its phonon-like character and, hence, the stronger the

influence of τ_{SO} rather than of τ_e. Thus, SPPP$_4$, that runs close to $\omega_{hBN}^{TO,\perp}$ within the studied k range, presents a little influence of any enhancement in τ_e produced by an increment in the mobility.

The ΔT^{TM} spectra are also strongly modulated by the thickness of the h-BN interlayer. Figure 6 shows the ΔT^{TM} spectra associated to the different SPPP and HPPP modes appearing in the dispersion curves of figure 4 for a k value corresponding to $\lambda_{SAW} = 250\,nm$. It can be seen that, increasing the h-BN thickness from 1 to 70 nm, SPPP$_1$, figure 6(a), and SPPP$_4$, figure 6(c), present stronger peaks that blue shift. The opposite trend is observed though for SPPP$_3$, figure 6(b), where the peak intensity decreases and the peak position red shifts when increasing the h-BN thickness from 1 nm to 50 nm. This later behaviour is due to the fact that SPPP$_3$ is strongly related to the SO phonon in AlN, and the electron-phonon coupling strength reduces as $exp(-2kd)$, as shown in equation (4). For a h-BN thickness of 70 nm, the SPPP$_2$ appears instead of SPPP$_3$, as shown in figures 4(e) and (f).

In addition to the tunability of the SPPP$_i$ and the HPPP$_i$ dispersion in the graphene/h-BN/AlN system provided by the thickness of the h-BN interlayer, graphene presents an intrinsic degree of tunability by means of the modulation of its carrier density n, or $E_F = \hbar v_F \sqrt{\pi n}$, through electrostatic gating. All SPPP$_i$ and HPPP$_i$ blue shift as the E_F increases, as expected from the hybridization with a higher energy graphene plasmon. However, the intensity of a particular SPPP$_i$ or HPPP$_i$ is especially enhanced at certain h-BN film thickness and E_F combinations. Therefore, a detailed study of the dispersion of the graphene/h-BN/AlN system, both in terms of h-BN thickness as well as graphene doping, is required for the design of the most efficient SAW-mediated plasmonic devices.

Figure 7 shows the evolution of the strength (expressed as the maximum value of the peak in the ΔT^{TM} spectra) of the different SPPP$_i$ and HPPP$_i$ induced by a SAW with $\lambda_{SAW} = 250\,nm$ for E_F varying from 0.1 eV to 0.6 eV and for different thicknesses of the h-BN interlayer. For thin h-BN films, the maximum of SPPP$_1$, figure 7(a), occurs at energies below ω_{AlN}^{TO} as the SPPP$_1$ cannot propagate into the reststrahlen band of AlN. However, for thicker h-BN layers, this boundary
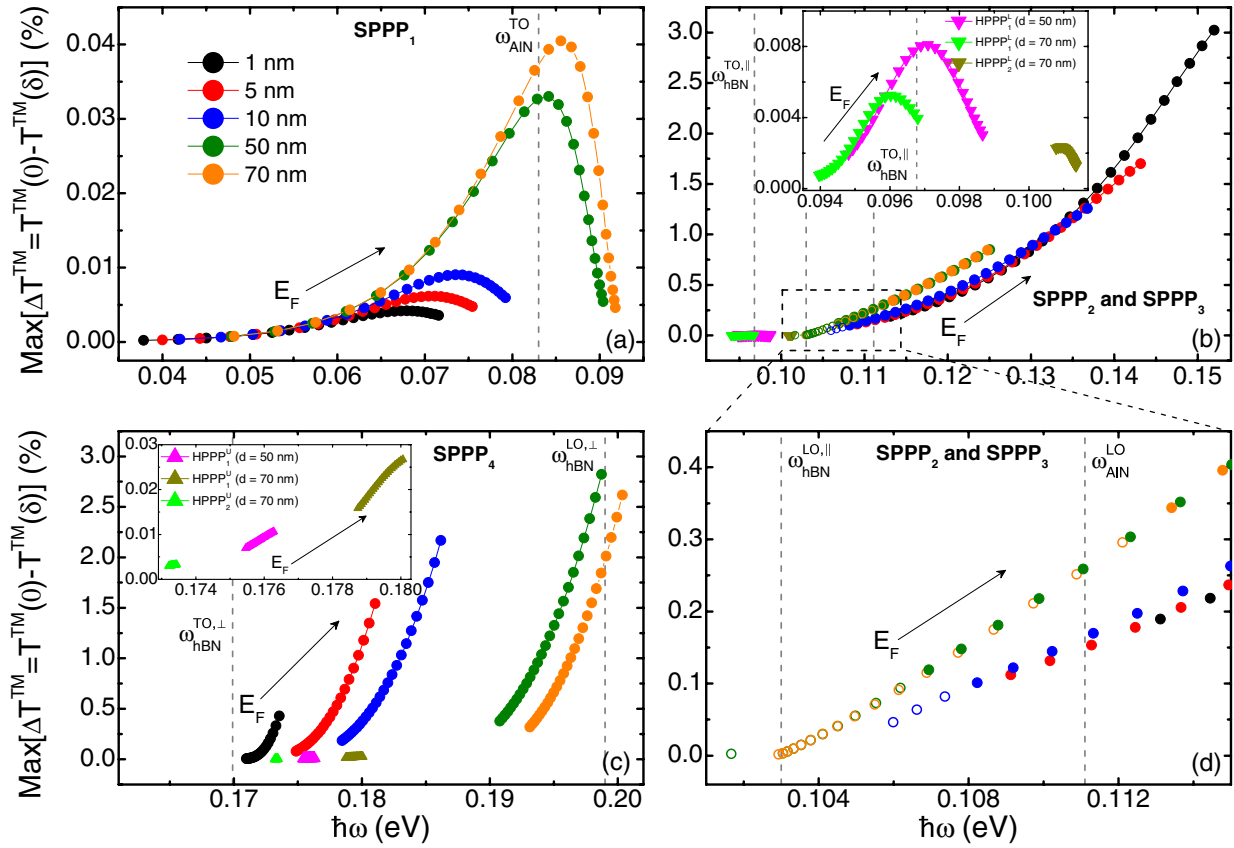
Figure 7. Evolution of the strength (expressed as the maximum value of the peak in the ΔT^{TM} spectra) of (a) SPPP$_1$, (b) SPPP$_2$ and SPPP$_3$, and (c) SPPP$_4$ with E_F for graphene/h-BN/AlN systems with carrier mobility $\mu = 10\,000\,\mathrm{cm^2\,V^{-1}\,s^{-1}}$ and various h-BN film thickness d in the presence of a SAW ($m = 1$, $\delta = 4\,\mathrm{nm}$, and $\lambda_{\mathrm{SAW}} = 250\,\mathrm{nm}$). (d) Zoom-in view of the box in (b). The solid circles represent the SPPP$_3$ mode whereas hollow circles correspond to the SPPP$_2$ mode. Insets in (b) and (c) show magnified views of the modulation of the HPPP$_i^L$ and HPPP$_i^U$, respectively, that appear for the 50 and 70 nm thick h-BN interlayers. E_F varies in all cases from 0.1 to 0.6 eV in steps of 0.02 eV in the direction of the arrow.

condition relaxes and the maximum occurs at energies beyond ω_{AlN}^{TO} but below $\omega_{hBN}^{TO,\parallel}$, as now is the lower reststrahlen band of h-BN the one effectively limiting the propagation of SPPP$_1$. In all cases, the appearance of a maximum as E_F increases is related to the existence of two competing mechanisms, since a larger carrier density makes the plasmon stronger while its shift to higher energies is stopped by either one of the reststrahlen bands. The behaviour of SPPP$_2$ and SPPP$_3$, figure 7(b), is more complex as it is affected by both the AlN reststrahlen band and the lower reststrahlen band of h-BN. As shown in figure 2(c) for a 1-nm thick h-BN interlayer, SPPP$_2$ appears very close to $\omega_{hBN}^{LO,\parallel}$ and is very weak. In order to benefit from its large lifetime, it is required to increase the h-BN interlayer thickness above 10 nm, as shown in figure 7(b) and its magnified view in figure 7(d), while keeping E_F low. In this regime, SPPP$_2$ evolves from $\omega_{hBN}^{LO,\parallel}$ onwards as E_F increases. However, for the k value imposed by the selected SAW, there is a transition from SPPP$_2$ to SPPP$_3$ at a certain threshold value of E_F. The threshold value that produces this crossover increases with the h-BN thickness, as depicted in figure 7(d). The intensity of SPPP$_3$ increases monotonically in the E_F range studied as its upper limit, $\omega_{hBN}^{TO,\perp}$, is far. However,

increasing the h-BN thickness reduces the energy range covered by SPPP$_3$ as the influence of AlN in the graphene/h-BN/AlN heterostructure reduces. The inset of figure 7(b) shows the evolution of HPPP$_1^L$ and HPPP$_2^L$, which are only observed for the 50 and 70 nm-thick h-BN interlayers for the k value considered. These HPPP$_i^L$ modes are expected to be confined within the lower reststrahlen band of h-BN. However, it can be seen that HPPP$_1^L$ extends slightly below $\omega_{hBN}^{TO,\parallel}$. This seems to be related to the fact that the lower reststrahlen band of h-BN lies within the reststrahlen band of AlN, so that the lower limit imposed by $\omega_{hBN}^{TO,\parallel}$ relaxes. The exact mechanism behind this is still unclear. In case of SPPP$_4$, figure 7(c), its strength increases monotonically with increasing E_F for all h-BN thickness values, as no boundary condition limits it. Conversely, HPPP$_1^U$ and HPPP$_2^U$, which are only observed for the 50 and 70 nm-thick h-BN interlayers for the k value considered (inset of figure 7(c)), appear confined within the upper h-BN reststrahlen band. These HPPP$_i^U$ modes are thus expected to peak or saturate when evolving further towards $\omega_{hBN}^{LO,\perp}$, if a broader parameter range is considered. In summary, figure 7 shows that, within the range of the parameter space studied, the graphene/h-BN/AlN heterostructure provides SPPP$_3$ and

J. Phys. D: Appl. Phys. **51** (2018) 204004

R Fandan *et al*

SPPP$_4$ with the largest intensities (3%), whereas SPPP$_2$ is an order of magnitude weaker (0.3%) and SPPP$_1$ is two orders of magnitude weaker (0.04%). In terms of hyperbolic modes, the HPPP$_i^L$ are very weak (0.008%) though the HPPP$_i^U$ can reach intensities (0.03%) comparable to those of SPPP$_1$.

5. Conclusions

In conclusion, we have theoretically demonstrated that SAWs can be used to generate SPPPs and HPPPs in graphene/h-BN heterostructures on a piezoelectric substrate, such as AlN, where the SAW creates a dynamic virtual diffraction overcoming the wave vector mismatch of SPPPs and HPPPs with the incident light. Graphene electrons couple to surface phonons of both the h-BN interlayer and the AlN substrate providing a complex SPPP dispersion relation that strongly depends on the thickness of the h-BN film and can be modulated by varying the Fermi energy of graphene. In addition, hyperbolic phonons appear in the case of multilayer h-BN films that also couple with the graphene carriers leading to tunable HPPPs. The h-BN interlayer is demonstrated to not only significantly change the hybridized SPPP dispersion but also to enhance the SPPP lifetime, as compared to the simpler graphene/AlN system. The lifetime enhancement provided by the h-BN film is shown to be related to both the higher carrier mobility induced in graphene and the larger lifetime of the h-BN surface phonons. Therefore, the graphene/h-BN/AlN system provides an advantageous platform with greater plasmon robustness and tunability for future SAW-based plasmonic devices.

Acknowledgments

ORCID iDs

R Fandan ⬤ https://orcid.org/0000-0002-4885-8853
J Schiefele ⬤ https://orcid.org/0000-0002-6422-0200
J Martínez ⬤ https://orcid.org/0000-0002-5912-1128
F Calle ⬤ https://orcid.org/0000-0001-7869-6704

References

[1] Maier S A 2007 *Plasmonics: Fundamentals and Applications* (Berlin: Springer)
[2] Ozbay E 2006 Plasmonics: merging photonics and electronics at nanoscale dimensions *Science* **311** 189–93
[3] Schuller J, Barnard E, Cai W, Jun Y, White J and Brongersma M 2010 Plasmonics for extreme light concentration and manipulation *Nat. Mater.* **9** 193–204
[4] Fernández-Domínguez A, García-Vidal F and Martín-Moreno L 2017 Unrelenting plasmons *Nat. Photon.* **11** 8–10
[5] Fang Y and Sun M 2015 Nanoplasmonic waveguides: towards applications in integrated nanophotonic circuits *Light Sci. Appl.* **4** e294
[6] Brongersma M and Kik P 2007 *Surface Plasmon Nanophotonics* (Berlin: Springer)
[7] Shalaev V 2007 Optical negative-index metamaterials *Nat. Photon.* **1** 41–8
[8] Yu N and Capasso F 2014 Flat optics with designer metasurfaces *Nat. Mater.* **13** 139–50
[9] Tame M, McEnery K, Özdemir Ş, Lee J, Maier S and Kim M 2013 Quantum plasmonics *Nat. Phys.* **9** 329–40
[10] Jablan M, Buljan H and Soljačić M 2009 Plasmonics in graphene at infrared frequencies *Phys. Rev.* B **80** 245435
[11] Khurgin J 2015 How to deal with the loss in plasmonics and metamaterials *Nat. Nanotechnol.* **10** 2–6
[12] Yan H, Low T, Zhu W, Wu Y, Freitag M, Li X, Guinea F, Avouris P and Xia F 2013 Damping pathways of mid-infrared plasmons in graphene nanostructures *Nat. Photon.* **7** 394–9
[13] Hwang E, Sensarma R and Das Sarma S 2010 Plasmon-phonon coupling in graphene *Phys. Rev.* B **82** 195406
[14] Garcia de Abajo F 2013 Graphene nanophotonics *Science* **339** 917–8
[15] Koppens F, Chang D and García de Abajo F 2011 Graphene plasmonics: a platform for strong light-matter interactions *Nano Lett.* **11** 3370–7
[16] Rivera N, Kaminer I, Zhen B, Joannopoulos J and Soljačić M 2016 Shrinking light to allow forbidden transitions on the atomic scale *Science* **353** 263–9
[17] Vakil A and Engheta N 2011 Transformation optics using graphene *Science* **332** 1291–4
[18] Christensen J, Manjavacas A, Thongrattanasiri S, Koppens F and García de Abajo F 2011 Graphene plasmon waveguiding and hybridization in individual and paired nanoribbons *ACS Nano* **6** 431–40
[19] Gullans M, Chang D, Koppens F, de Abajo F and Lukin M 2013 Single-photon nonlinear optics with graphene plasmons *Phys. Rev. Lett.* **111** 247401
[20] Rodrigo D, Limaj O, Janner D, Etezadi D, Garcia de Abajo F, Pruneri V and Altug H 2015 Mid-infrared plasmonic biosensing with graphene *Science* **349** 165–8
[21] Grigorenko A, Polini M and Novoselov K 2012 Graphene plasmonics *Nat. Photon.* **6** 749–58
[22] Chen J *et al* 2012 Optical nano-imaging of gate-tunable graphene plasmons *Nature* **487** 77–81
[23] Fei Z *et al* 2012 Gate-tuning of graphene plasmons revealed by infrared nano-imaging *Nature* **487** 82–5
[24] Dai S *et al* 2015 Graphene on hexagonal boron nitride as a tunable hyperbolic metamaterial *Nat. Nanotechnol.* **10** 682–6
[25] Constant T, Hornett S, Chang D and Hendry E 2015 All-optical generation of surface plasmons in graphene *Nat. Phys.* **12** 124–7
[26] Luxmoore I, Gan C, Liu P, Valmorra F, Li P, Faist J and Nash G 2014 Strong coupling in the far-infrared between graphene plasmons and the surface optical phonons of silicon dioxide *ACS Photonics* **1** 1151–5
[27] Yan H, Li X, Chandra B, Tulevski G, Wu Y, Freitag M, Zhu W, Avouris P and Xia F 2012 Tunable infrared plasmonic devices using graphene/insulator stacks *Nat. Nanotechnol.* **7** 330–4

J. Phys. D: Appl. Phys. 51 (2018) 204004

R Fandan *et al*

[28] Gao W, Shu J, Qiu C and Xu Q 2012 Excitation of plasmonic waves in graphene by guided-mode resonances *ACS Nano* **6** 7806–13

[29] Gao W, Shi G, Jin Z, Shu J, Zhang Q, Vajtai R, Ajayan P, Kono J and Xu Q 2013 Excitation and active control of propagating surface plasmon polaritons in graphene *Nano Lett.* **13** 3698–702

[30] Schiefele J, Pedrós J, Sols F, Calle F and Guinea F 2013 Coupling light into graphene plasmons through surface acoustic waves *Phys. Rev. Lett.* **111** 237405

[31] Farhat M, Guenneau S and Bağcı H 2013 Exciting graphene surface plasmon polaritons through light and sound interplay *Phys. Rev. Lett.* **111** 237404

[32] Kim S *et al* 2015 Synthesis of large-area multilayer hexagonal boron nitride for high material performance *Nat. Commun.* **6** 8662

[33] Banszerus L, Schmitz M, Engels S, Dauber J, Oellers M, Haupt F, Watanabe K, Taniguchi T, Beschoten B and Stampfer C 2015 Ultrahigh-mobility graphene devices from chemical vapor deposition on reusable copper *Sci. Adv.* **1** e1500222

[34] Dean C *et al* 2010 Boron nitride substrates for high-quality graphene electronics *Nat. Nanotechnol.* **5** 722–6

[35] Caldwell J *et al* 2014 Sub-diffractional volume-confined polaritons in the natural hyperbolic material hexagonal boron nitride *Nat. Commun.* **5** 5221

[36] Dai S *et al* 2014 Tunable phonon polaritons in atomically thin van der Waals crystals of boron nitride *Science* **343** 1125–9

[37] Gan C, Chu H and Li E 2012 Synthesis of highly confined surface plasmon modes with doped graphene sheets in the midinfrared and terahertz frequencies *Phys. Rev.* B **85** 125431

[38] Ng S, Hassan Z and Abu Hassan H 2007 Experimental and theoretical studies of surface phonon polariton of AlN thin film *Appl. Phys. Lett.* **90** 081902

[39] Kazan M, Pereira S, Correia M and Masri P 2009 Directional dependence of AlN intrinsic complex dielectric function, optical phonon lifetimes, and decay channels measured by polarized infrared reflectivity *J. Appl. Phys.* **106** 023523

[40] Castro E, Ochoa H, Katsnelson M, Gorbachev R, Elias D, Novoselov K, Geim A and Guinea F 2010 Limits on charge carrier mobility in suspended graphene due to flexural phonons *Phys. Rev. Lett.* **105** 266601

[41] Amorim B and Guinea F 2013 Flexural mode of graphene on a substrate *Phys. Rev.* B **88** 115418

[42] Tomadin A, Principi A, Song J, Levitov L and Polini M 2015 Accessing phonon polaritons in hyperbolic crystals by angle-resolved photoemission spectroscopy *Phys. Rev. Lett.* **115** 087401

[43] Hwang E and Das Sarma S 2007 Dielectric function, screening, and plasmons in two-dimensional graphene *Phys. Rev.* B **75** 205418

[44] Wunsch B, Stauber T, Sols F and Guinea F 2006 Dynamical polarization of graphene at finite doping *New J. Phys.* **8** 318

[45] Zhan T, Shi X, Dai Y, Liu X and Zi J 2013 Transfer matrix method for optics in graphene layers *J. Phys.: Condens. Matter* **25** 215301

[46] Lean E G 1973 *Progress in Optics* vol XI, ed E Wolf (Amsterdam: North-Holland) p 123

[47] Shilton R, Tan M, Yeo L and Friend J 2008 Particle concentration and mixing in microdrops driven by focused surface acoustic waves *J. Appl. Phys.* **104** 014910

[48] Laude V, Gérard D, Khelfaoui N, Jerez-Hanckes C F, Benchabane S and Khelif A 2008 Subwavelength focusing of surface acoustic waves generated by an annular interdigital transducer *Appl. Phys. Lett.* **92** 094104